PHYSICAL REVIEW B VOLUME 16, NUMBER 8 15 OCTOBER 1977

Intraband Raman scattering by free carriers in heavily doped n-Si

Meera Chandrasekhar† and Manuel Cardona
Max-Planck-Institut für Festkörperforschung, 7 Stuttgart 80, Federal Republic of Germany

Evan O. Kane*
Max-Planck-Institut für Festkörperforschung, 7 Stuttgart 80, Federal Republic of Germany and Bell Laboratories, Murray Hill, New Jersey 07974

(Received 16 May 1977)

Intraband Raman scattering from free carriers in n-type Si has been studied at high-impurity concentrations (10^{19}–10^{20} cm^{-3}). A strong low-frequency tail attributed to intervalley fluctuations is observed. This tail extends to 200 cm^{-1} and obeys the same selection rules as the scattering between valley-orbit split donor levels. The strength of the tail is found to be independent of exciting frequency. A theoretical study of free-carrier intervalley fluctuations, as has been previously formulated, yields results that are in contradiction with the line shape of the tail and the above experimental observations. The observed scattering cross section is also an order of magnitude larger than that predicted by theory. *Ad hoc* phenomenological models are proposed which remove some but not all of the contradictions discussed above. The strongest evidence for an intervalley mechanism is provided by measurements under uniaxial stress. Large static uniaxial stresses (up to 20 kbar) were applied along the [001], [111], and [110] crystallographic directions. The results are qualitatively understood on the basis of the simplified *ad hoc* models and of transverse mass anisotropies induced by the splitting of X_1 points by [111] and [110] uniaxial stresses. The contradictions between the present theory and experiment suggest the inadequacy of a free-carrier treatment in the high-impurity regime.

I. INTRODUCTION

In heavily doped n-type Si, ($n = 10^{19}$–10^{20} cm^{-3}), the partial filling of the ⟨100⟩ conduction-band valleys gives rise to free-carrier excitations that can be observed in Raman scattering. Effects due to intra- and interband scattering may be seen. The intraband scattering produces a broad low-frequency tail, while the interband excitations from the $\Delta_1 \rightarrow \Delta_2'$ conduction bands produce an interference with the zone-center optical phonon at 520 cm^{-1} (Fano effect).[1] In this paper, we restrict ourselves to the discussion of intraband scattering, the Fano effect being treated in a separate publication.

We have investigated the low-frequency tail due to intraband scattering for electron concentrations of 1.5×10^{19} cm^{-3} and 1.5×10^{20} cm^{-3}. The tail has been observed before at lower concentrations in Si (1.7×10^{18}),[2] and Ge (1.7×10^{17}),[3] and has been attributed to intervalley electron density fluctuations, the theoretical description for which has been given by Platzman[4] and Klein.[5] We discuss and extend this theory using a free-electron approach to derive selection rules for intervalley fluctuations that are different from the simpler selection rules for valley-orbit scattering (Γ_{12} in Si). The experiments, however, are in contradiction with the selection rules derived by the theory, and agree better with the valley-orbit selection rules. We have also attempted to fit the line shape of the tail in the light of the theory, and find that the strong divergence of the line shape predicted by the theory for low frequencies (<100 cm^{-1}) is not followed by the experimental tail, a possible consequence of multiple scattering. The dependence of this interband scattering on the exciting frequency ω_L was also investigated. Within the frequency range at hand (1.6–2.5 eV) it was found to be independent of frequency. The standard ω_L^4 dependence found for scattering by phonons in the nonresonant region was not observed for the free-electron scattering.

The strongest evidence of the tail being related to intervalley charge-density fluctuations is given by uniaxial-stress experiments.[6] Large static uniaxial stresses (up to 20 kbar) were applied along the [100] and [111] crystallographic directions for both concentrations (1.5×10^{19} and 1.5×10^{20} cm^{-3}) and the [110] direction for the lower concentration: the scattering tail disappears as all the carriers are transferred to one valley by application of a uniaxial stress. These results indicate that the mechanism is of an intervalley nature, although the exact description is not given by the theory. The free-electron approach normally used seems to be inadequate for the heavily doped semiconductors under consideration, for which the lifetime broadening is of the order of the Fermi energy.

Section II of this paper gives a short survey of the experimental details. The theory is presented in Sec. III, while Sec. IV deals with the experimental results and their interpretation: our study

consists of an analysis of the selection rules, scattering line shape, measurements under uniaxial stress, dependence on exciting frequency and a discussion of the observed electronic scattering efficiency as compared with the efficiency for scattering by the optical phonon. Section V gives the conclusions.

II. EXPERIMENTAL DETAILS

Raman spectra were taken at room temperature using the back-scattering geometry standard for opaque samples. Spectra physics and coherent radiation Ar^+ and Kr^+ lasers were used for the exciting radiation. All measurements under uniaxial stress were done using 300–600 mW of 6471 Å radiation from a Kr^+ laser. A Spex-triple or Spex-double monochromator with holographic gratings and a cooled photomultiplier equipped with photon counting electronics were used for detection. Data was stored on a multichannel analyzer. Counting times from 5 to 50 sec were used, the longer counting times for polarization parallel to the slit in the red region where the grating efficiency was poor.

The stress apparatus used, provided with digital readout, has been described in the literature.[7] Typical compressive stresses up to 20 kbar could be reached.

Samples were cut from single crystals of Si and x-ray oriented to within 1°. Typical dimensions were $20\times1.3\times1.3$ mm^3, the stress applied along the long dimension. The face used for Raman scattering was polished to optical flatness with 0.3-μ alumina, polish-etched with Syton for 10 min and etched in HF for 1 min. Care was taken to minimize fine hairline scratches and hence scattered light near the laser line, in order to make measurements on the tail reliable. The carrier concentrations of the samples as quoted were determined by measuring the resistivity with a four-probe technique. The relationship between resistivity and electron concentration were found from Ref. 8.

III. THEORY

We discuss Raman scattering from electrons at high concentration in the multivalley free-carrier model. We follow the derivation of density-fluctuation scattering (intervalley fluctuations) first given by Platzman[4] as reported by Klein.[5]

Rewriting Klein's Eq. (4.117a)[5] we have an expression for the Raman efficiency per unit scattering length:

$$\frac{d^2R}{d\omega\, d\Omega}=K(1+n_\omega)\,\mathrm{Im}\left(\sum_i(\mu_i^2F_i)-v_q\sum_{i<j}(\mu_i-\mu_j)^2F_iF_j\right)\epsilon^{-1}, \tag{1}$$

where the dielectric constant ϵ is given by

$$\epsilon=\epsilon_\infty-v_q\sum_j F_j\,, \tag{2}$$

with the following definitions

$$v_q=4\pi e^2/q^2\,, \tag{3}$$

$$\mu_j=\vec{e}_1\cdot\vec{\mu}_j\cdot\vec{e}_2\,, \tag{4}$$

$$n_\omega=[\exp(\hbar\omega/kT)-1]^{-1}\,, \tag{5}$$

$$K=\left(\frac{e^2}{mc^2}\right)^2\frac{\hbar}{\pi}S\,. \tag{6}$$

The resonant factor S equals one for photon energies away from resonant gaps, a condition which should hold in our case ($\hbar\omega\simeq2$ eV, resonant gap $\simeq4.5$ eV). In Eq. (4) $\vec{\mu}_j$ is the reciprocal mass tensor in units of the free electron mass. $\vec{q}$ and ω are the momentum and frequency transfer between the incident photon (polarization $\vec{e}_1$) and scattered photon, $\vec{e}_2$. The dielectric constant ϵ and F_j are to be evaluated at $\vec{q}$ and ω. The indices i and j are summed over valleys. ϵ_∞ is the background dielectric constant, for silicon ~12 at the $\vec{q}$ and ω of this problem. This ϵ_∞ will be seen to be small compared to ϵ from the free carriers. In principle the background electrons responsible for ϵ_∞ should also be included in the bracketed term but we neglect this small contribution.

The problem then is to derive an expression for the polarizability, F_j, of a single valley in the presence of strong impurity scattering. We use a plane wave basis and follow the procedure of Kohn and Luttinger[9] to derive an expression for the density matrix $\langle\vec{k}+\vec{q}\,|\rho|\,\vec{k}\rangle$ which we abbreviate as ρ_k. In Eq. (A6) of Appendix A we show that ρ_k is given by

$$\rho_k=\frac{(f_{\vec{k}}^{0}-f_{\vec{k}}^{0\prime})\phi(q)+iWn_E}{\hbar\omega-E_k'+E_k+i\hbar/\tau_E}\,, \tag{7}$$

where

$$\vec{k}'=\vec{k}+\vec{q}\,, \tag{8}$$

$$\hbar\tau_E^{-1}=W\sum_{\vec{k}''}\delta(E-\mathcal{E}_{\vec{k}''})=W\rho_s(E)\,, \tag{9}$$

$$n_E=\sum_{\vec{k}''}\delta(E-\mathcal{E}_{\vec{k}''})\rho_{\vec{k}''};\quad E=\mathcal{E}_{\vec{k}}\,. \tag{10}$$

The scattering has been assumed to be elastic and independent of momentum transfer $\vec{k}-\vec{k}''$ in Eqs. (9) and (10). The approximation is not too

good for impurity scattering except in the limit of short screening lengths, but is made to simplify the algebra. We do not believe it will have a major influence on our results since τ_E will be taken from experimental values of the conductivity.

E_k is the carrier energy, assumed parabolic with an ellipsoidal mass tensor. f_k^0 is the Fermi distribution and $\phi(q)$ is the total potential driving the electrons. $W = 2\pi V^2$, where $V = |H_{k-k'}|$ is an average impurity scattering matrix element. n_E is the perturbed charge density in the energy interval dE at E. The term involving n_E in Eq. (7) comes from the effect of collisions "scattering into" the momentum space point $\vec{k}$ whereas $1/\tau_E$ corresponds to "scattering out." The "scattering in" term is equivalent to the correction due to relaxation to the local equilibrium density in the more phenomenological description of Mermin.[10]

In order to calculate n_E we substitute Eq. (7) in Eq. (10) obtaining the result

$$n_E = -\frac{\partial f_0}{\partial E}\frac{\phi B_1}{1 - iWB_2}, \tag{11}$$

where

$$B_1 = \sum_{\vec{k}} \frac{\delta(E - \mathcal{E}_{\vec{k}})\,\vec{q}\cdot\nabla_{\vec{k}}\mathcal{E}_{\vec{k}}}{\hbar\omega - \vec{q}\cdot\nabla_{\vec{k}}\mathcal{E}_{\vec{k}} + i\hbar/\tau_E}, \tag{12}$$

$$B_2 = \sum_{\vec{k}} \frac{\delta(E - \mathcal{E}_{\vec{k}})}{\hbar\omega - \vec{q}\cdot\nabla_{\vec{k}}\mathcal{E}_{\vec{k}} + i\hbar/\tau_E}. \tag{13}$$

In obtaining (11) we have also made the approximations

$$f^0_{k'} - f^0_k = \frac{\partial f_0}{\partial E}\vec{q}\cdot\nabla_{\vec{k}}\mathcal{E}_{\vec{k}} \tag{14}$$

$$\mathcal{E}_{\vec{k}'} - \mathcal{E}_{\vec{k}} = \vec{q}\cdot\nabla_{\vec{k}}\mathcal{E}_{\vec{k}} \tag{15}$$

which are justified since $q \ll k_F$. In evaluating Eqs. (12) and (13) it is convenient, although not necessary, to expand the denominators in powers of $\vec{q}\cdot\nabla_{\vec{k}}\mathcal{E}_{\vec{k}}/(\hbar\omega + i\hbar/\tau_E)$. This is also a good approximation since $qk_F/m^* \ll \hbar/\tau_E$. Equations (12) and (13) are then further simplified to

$$B_1 = d/(\hbar\omega + i\hbar/\tau_E)^2, \tag{16}$$

$$B_2 = \frac{\rho_s(E)}{(\hbar\omega + i\hbar/\tau_E)} + \frac{d}{(\hbar\omega + i\hbar/\tau_E)^3}, \tag{17}$$

where

$$d = \sum_{\vec{k}} \delta(E - \mathcal{E}_{\vec{k}})(q\cdot\nabla_{\vec{k}}\mathcal{E}_{\vec{k}})^2. \tag{18}$$

Making a parabolic approximation for $\mathcal{E}_{\vec{k}}$ it is easy to derive an expression for d and for the density of states, $\rho_s(E)$, of a single valley without spin.

$$\rho_s(E) = (m_x m_y m_z)^{1/2}(2E)^{1/2}/2\pi^2\hbar^3, \tag{19}$$

$$d = \rho_s(E)(\tfrac{2}{3}E)\hbar^2\left(\frac{q_x^2}{m_x} + \frac{q_y^2}{m_y} + \frac{q_z^2}{m_z}\right). \tag{20}$$

Substitution of these results for B_1, B_2 in Eq. (11) and use of Eq. (9) allows us to write Eq. (11) as

$$\frac{n_E}{\phi} = -\frac{(\partial f_0/\partial E)(\frac{2}{3}E)\rho_s(E)Q}{(\hbar\omega + i\hbar/\tau_E)\left[\hbar\omega - i(\frac{2}{3}E)(\hbar/\tau_E)\,Q/(\hbar\omega + i\hbar/\tau_E)^2\right]}, \tag{21}$$

where

$$Q = \hbar^2\left(\frac{q_x^2}{m_x} + \frac{q_y^2}{m_y} + \frac{q_z^2}{m_z}\right). \tag{22}$$

The polarizability F for a given ellipsoid in Eq. (1) is then given by integrating Eq. (21) over energy

$$F = 2\int dE\, n_E/\phi, \tag{23}$$

where the factor 2 is for spin.

In Eq. (21) the derivative of the Fermi function $\partial f_0/\partial E$ gives a δ-function at the Fermi surface at low temperatures.

For $n_0 = 1.5\times10^{19}/\mathrm{cm}^3$ we have $E_F = 21$ meV $\simeq kT_{\mathrm{room}}$. However, the selection rules have little temperature dependence between room temperature and liquid nitrogen so that for simplicity we will discuss Eq. (21) evaluated at the low temperature Fermi level.

Using Eq. (19) for $\rho_s(E)$ it is easy to show

$$-\int 2\frac{\partial f_0}{\partial E}\left(\frac{2E}{3}\right)\rho_s(E)\,dE = \frac{n_0}{\nu}, \tag{24}$$

where ν is the number of ellipsoids and n_0/ν is the total carrier density per ellipsoid. Equations (21) and (23) then give

$$F_j = \left(\frac{n_0}{\nu}\right)Q_j\left[\left(\hbar\omega + \frac{i\hbar}{\tau_{EF}}\right) \times \left(\hbar\omega - \frac{i(2E_F/3)(\hbar/\tau_{EF})Q_j}{(\hbar\omega + i\hbar/\tau_{EF})^2}\right)\right]^{-1}, \tag{25}$$

where Q_j is defined in Eq. (22).

We now wish to estimate the factors entering in Eq. (25) in order to apply Eq. (25) to the Raman cross-section formula in Eq. (1).

We use the dc conductivity to determine the scattering time at the Fermi surface, τ_{EF}. By a completely analogous calculation we evaluate the dc conductivity to be

$$\sigma^j_{xx} = (n_0/\nu)e^2\tau_{EF}/m^j_x. \tag{26}$$

Equation (26) can also be derived directly from Eq. (25) using

$$\sigma_{xx} = i\omega(\epsilon_{xx} - 1)/4\pi \tag{27}$$

and taking $q \to 0$ followed by $\omega \to 0$. Summing over

all ellipsoids and using $\sigma\,(1.5\times10^{19}/\mathrm{cm}^3)=250\ \Omega^{-1}\mathrm{cm}^{-1}$ we obtain $\tau_{EF}=1.5\times10^{-14}$ sec, $\hbar/\tau_{EF}=43$ meV. As mentioned earlier $E_F\,(1.5\times10^{19})=21$ meV, $\hbar\omega(100\ \mathrm{cm}^{-1})=12.4$ meV. To evaluate Q in Eq. (22) we take $q=2(2\pi/\lambda)n$, $n=\sqrt{15}$, $\lambda=6471$ Å. Then $\hbar^2q^2(\frac{2}{3}m_t+\frac{1}{3}m_l)=1.66$ meV using $m_t=0.1905m_0$, $m_l=0.9163m_0$,[11] the transverse and longitudinal masses of the effective mass ellipsoid. We also estimate $\epsilon(q,\omega)=\epsilon_\infty+190$.

It is then easy to see with the parameters just given that the term in Q_j in the denominator of Eq. (25) is negligible compared to $\hbar\omega$. If we also neglect ϵ_∞ compared to $-v_q\sum_q F_j=190$, we can write Eq. (1)

$$\frac{d^2R}{d\omega\,d\Omega}=\left(\frac{e^2}{mc^2}\right)^2\frac{\hbar}{\pi}(1+n_\omega)\times\mathrm{Im}\left(\frac{(n_0/\nu)\sum_{i<j}(\mu_i-\mu_j)^2Q_iQ_j}{\hbar\omega(\hbar\omega+i\hbar/\tau_{EF})\sum_j Q_j}\right).\qquad(28)$$

Equation (28) signifies that the scattering cross section is obtained from the directions of the incident and scattered fields and the scattering wave vector $\vec{q}$ by contracting with an eighth rank tensor. In contrast, the standard $\vec{q}$-independent scattering selection rules are determined by a fourth-rank tensor. We have not been able to express Eq. (28) as the square of a fourth-rank tensor contracted with the field directions and twice $\vec{q}$. If Q_iQ_j is neglected in the numerator of Eq. (28), the scattering cross section can be represented by the square of a second-rank tensor.

The theoretical values of the relative scattering cross section given in Table I have been calculated using Eq. (28) with the further approximation that $m_t/m_l=0$. The one case where this approximation gives zero has been evaluated for the actual ratio $m_t/m_l=0.21$.

If we leave out the factors Q_iQ_j in Eq. (28) we obtain the same selection rules as for scattering between the valley-orbit split lower levels of donors ($\vec{q}$-independent Raman tensor, Γ_{12} symmetry for Si). These corresponding relative scattering intensities are also listed in Table I. The two sets of rules are distinctly different for the configuration $[001]([110],[1\bar{1}0])[00\bar{1}]$. As we see in Table I the experiment clearly favors the valley-orbit model.

In addition to this disagreement with the free-carrier theory, the observed ω dependence does not follow $(1/\omega)[1+n(\omega)]$ as predicted by the theory. The low-frequency divergence of this function is not found experimentally. At the same time the appearance of $q\sim2\omega_L/c=4\pi/\lambda_L$ (ω_L is the exciting laser's frequency) in the Q's of Eq. (28) introduces a proportionality to ω_L^2 in the scattering efficiency which is also not observed.

We can derive a more suitable phenomenological theory in a somewhat arbitrary manner by introducing a dimensionless function $a(\omega)$ in Eq. (25), to make the second term in brackets in the denominator dominate the $h\omega$ term in order to eliminate the Q dependence of the scattering efficiency. This is not too unreasonable since with $\hbar/\tau_{EF}\gg E_F$ we cannot expect quantitative values from a free electron theory treating the scattering as a small perturbation. With this change the analog of Eq. (28) becomes

$$\frac{d^2R}{d\omega\,d\Omega}=\left(\frac{e^2}{mc^2}\right)^2\frac{\hbar}{\pi}(1+n_\omega)\left(\frac{n_0}{\nu^2}\right)\times\sum_{i<j}(\mu_i-\mu_j)^2\frac{\hbar\omega}{a(\omega)(2E_F/3)\hbar/\tau_{EF}}.\qquad(28a)$$

Of course, we have no estimate for the *ad hoc* function $a(\omega)$ from first principles but we can determine empirically that the functional form

$$a(\omega)=a_0[1+(\hbar\omega/E_a)^2]\qquad(28b)$$

provides a suitable fit to the ω-dependence of the experimental scattering efficiencies if E_a is taken to be of the order of 8 meV. Equation (28a) gives the same selection rules as valley-orbit scattering, and removes all dependence on exciting frequency, in agreement with experiment.

In order to give a better understanding of what has been done here we note that if we assume $\hbar\omega\ll\hbar/\tau_{EF}$, which is quite accurate, Eq. (25) can be derived from a classical calculation in which the Q_j term in the denominator comes from the effect of diffusion (using Fermi-Dirac rather than Boltzmann statistics). Equation (28a) assumes that the diffusion current dominates the net rate of change of particle density so that the distribution is nearly in equilibrium in the applied potential at all times. The cancellation of the Q_j factors is then a simple consequence of the fact that the equilibrium density depends on the density of states but not on the direction of the applied potential (beating potential of the two light beams). Unfortunately, as we shall see in Sec. IV E, the absolute values of $d^2R/d\omega\,d\Omega$ predicted with Eq. (28a) using $a_0=1$ are smaller than the already low value given by Eq. (28), in complete disagreement with experiment. Again this could be solved in an *ad hoc* fashion by taking $a_0\ll1$. This ansatz, however, may be difficult to justify in view of the fact that we are neglecting the term containing $\hbar\omega$ in the denominator of Eq. (25).

There is yet another heuristic approach possible to remove the shortcomings of Eq. (28). Experi-

ments indicate that the dependence on the direction and magnitude of $\vec{q}$ must be removed from that equation. The electron mean free path in our samples is $l \sim 25$ Å. Under these conditions it is questionable to what extent the $\vec{k}$ conservation required by the free electron theory may hold. If one looks for an isotropic λ_L-independent quantity with which to replace $\vec{q}$ in Eqs. (22) and (28), one naturally encounters $2\pi/l$, which is much larger than $4\pi/\lambda_L$. This *ad hoc* substitution gives us both the right selection rules and exciting frequency dependence. The line shape problem, however, is not solved, nor that of scattering efficiency, for which the substitution increases the value estimated by Eq. (28) by three orders of magnitude, now *too large* as compared with experiment.

IV. EXPERIMENTAL RESULTS AND DISCUSSION

Low-frequency tails due to intraband scattering were observed in configurations that allow valley-orbit (Γ_{12}) symmetry. An example of typical experimental data is given in Fig. 1, where Raman spectra in the 20–700 cm^{-1} Stokes region for Si ($n = 1.5\times10^{19}$ cm^{-3}) are shown for three exciting frequencies of 4880, 5145, and 6471 Å. Standard notation is used to describe the scattering configurations, e.g., $x(yz)\bar{x}$, where x and $\bar{x}$ are the

TABLE I. Selection rules and scattering efficiency for intervalley fluctuations and valley orbit scattering. Experimental values for Si ($n = 1.5 \times 10^{19}$ cm^{-3}). Intervalley selection rules are calculated assuming $m_t/m_l = 0$, except in the cases noted (b).

		Selection rules			
	Configuration		Valley-orbit	Experimental at [a]	
$\vec{q}, p_1, p_2$	$\vec{q}(\vec{e}_1\vec{e}_2)(-\vec{q})$	Intervalley	(Γ_{12})	50 cm^{-1}	100 cm^{-1}
$\vec{q} = (0,0,1)$	(a) (p_1p_1)	(0.4) [b]	1	0.8	1.0
$\vec{p}_1 = \frac{1}{\sqrt{2}}(1,1,0)$	(b) (p_1p_2)	4	3	2.8	3.0
$\vec{p}_2 = \frac{1}{\sqrt{2}}(1,\bar{1},0)$	(c) (p_2p_2)	(0.4) [b]	1	0.8	1.0
$\vec{q} = (0,0,1)$	(d) (p_1p_1)	4	4	3.8	3.7
$\vec{p}_1 = (1,0,0)$	(e) (p_1p_2)	0	0	0	0
$\vec{p}_2 = (0,1,0)$	(f) (p_2p_2)	4	4	3.8	3.7
$\vec{q} = \frac{1}{\sqrt{2}}(1,1,0)$	(g) (p_1p_1)	1	1	1.0	1.0
$\vec{p}_1 = \frac{1}{\sqrt{2}}(1,\bar{1},0)$	(h) (p_1p_2)	0	0	0	0
$\vec{p}_2 = (0,0,1)$	(i) (p_2p_2)	4	4	3.5	4.1
$\vec{q} = \frac{1}{\sqrt{2}}(1,\bar{1},0)$	(j) (p_1p_1)	0	0	0	0
$\vec{p}_1 = \frac{1}{\sqrt{3}}(1,1,1)$	(k) (p_1p_2)	2	2	2.0	2.4
$\vec{p}_2 = \frac{1}{\sqrt{6}}(1,1,\bar{2})$	(l) (p_2p_2)	1	1	0.9	1.1

[a] Experimental values are calculated relative to row (g), except rows (a) and (c).

[b] Rows (a) and (c) have experimental values relative to row (d). Intervalley selection rules are calculated using $m_t/m_l = 0.21$. Scattering efficiency for intervalley scattering is zero for $m_t/m_l = 0$.

incident and scattered wave vectors, y and z the incident and scattered electric field vectors. x,y,z are defined in each figure. In the configuration chosen in Fig. 1, only Γ_1 and Γ_{12} components of the second-rank Raman tensor are allowed, hence the tail of Γ_{12} and the second-order acoustic phonons of Γ_1 symmetries appear, while the first-order optical phonon at 520 cm^{-1} of $\Gamma_{25'}$ symmetry is absent. The tail extends up to ~200 cm^{-1}, and is comparable in intensity to the 2TA(X) phonon peak at 300 cm^{-1}.

A. Selection rules

Selection rules and scattering efficiencies for intervalley fluctuations, as described in the theory [Eq. (28)] were calculated and compared to the valley-orbit selection rules for a number of different polarizations (see Table I). The selection rules for intervalley fluctuations were calculated (Table I, Column 3) using Eq. (28), setting $m_t/m_l = 0$ except in the cases noted in Table I (a and c). The valley orbit or Γ_{12} selection rules (Table I, Column 4) arise when the factors $Q_i Q_j$ are omitted from Eq. (28). The scattering cross section then reduces to

$$R \sim \frac{d^2R}{d\omega\, d\Omega} \sim \sum_{i<j} (\mu_i - \mu_j)^2 . \tag{29}$$

A nonzero scattering cross section, therefore, arises only when at least two ellipsoids contribute with different components of the mass tensor. This condition also holds if the $Q_i Q_j$ terms are included. This simple observation helps explain most of the behavior of the tail under uniaxial stress.

Though the selection rules calculated by the two methods agree for several polarizations, they are seen to differ in certain cases [configurations (a) to (c) in Table I]. The experimental scattering efficiencies relative to an arbitrarily chosen configuration [in this case, (g)], are also given in Table I for Stokes shifts of 50 and 100 cm^{-1}. They are seen to agree better with the valley orbit (Γ_{12}) scattering, particularly in the crucial cases (a) to (c). The experimental uncertainty is somewhat less for the 100 cm^{-1} data, where the agreement with valley-orbit scattering is within 15%, the order of the experimental error. Data for $n = 1.5\times10^{19}$ cm^{-3} are given in Table I. A similar determination of the relative scattering cross sections for experimental data at $n = 1.5\times10^{20}$ cm^{-3} is somewhat inaccurate owing to the difficulty in defining the background level arising from the Fano interaction that affects the optical phonon (see for example, Fig. 4). In addition, the higher Fermi level of 0.1 eV, close to the X point, produces nonparabolic effects that make theoretical calculations difficult.

We note here that both *ad hoc* assumptions outlined in Sec. III [Eq. (28a) and the replacement of q by $2\pi/l$] give the form of Eq. (29) for the scattering efficiency, and therefore the valley-orbit selection rules in agreement with experiment.

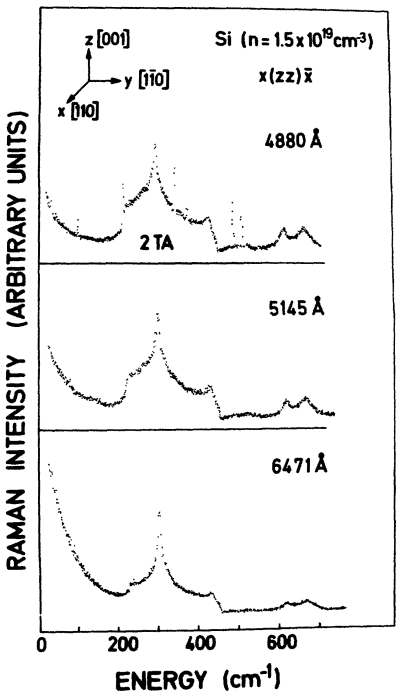

FIG. 1. Raman spectra at room temperature of n-type Silicon ($n = 1.5\times10^{19}$ cm^{-3}) for three exciting frequencies, 4880, 5145, and 6471 Å. Note the low frequency tail (of Γ_{12} symmetry) extending to 200 cm^{-1}. The second order acoustical phonons (of Γ_1 symmetry) are also present, while the zone center optical phonon of $\Gamma_{25'}$ symmetry is disallowed in the orientation used. The sharp peaks in the 4880 Å spectrum are due to plasma lines. The horizontal scale is linear in wavelength rather than wavenumber. Low-frequency air lines were eliminated by blowing helium gas over the sample for the first 150 cm^{-1}. Integration times of 5 sec were used for the 4880 and 5145 Å spectra, 10 sec for the 6471-Å spectra. The vertical scale was adjusted so that the 2TA(X) phonon at ~300 cm^{-1} has the same intensity for the three exciting frequencies.

B. Line shapes

An attempt was made to fit the experimental line shape of the tail to the product of the Bose factor $(1+n_\omega)$ and a power of the frequency shift ω

$$I(\omega) = \omega^{-m}(1+n_\omega) . \tag{30}$$

According to the discussion in Sec. III [Eq. (28)], m should have the value of 1 if $\omega\tau \ll 1$, higher otherwise. Unfortunately the value of $m = 1$ does not

give a good fit except at higher frequencies, where the data is not sufficiently accurate (Fig. 2, dashed lines). The strong divergence of Eq. (30) at low frequencies was not observed experimentally. It is possible that contributions from multiple scattering, neglected in Sec. III could affect the line shape and suppress the divergence produced by Eq. (30).

This divergence is also eliminated by the *ad hoc* assumption of Eqs. (28a) and (28b). Also plotted in Fig. 2 (solid line) is a fit using the frequency dependence predicted by these equations with $E_a = 8$ meV. The fit is seen to be quite good.

The second phenomenological approach outlined in Sec. III, that of replacing $\vec{q}$ by $2\pi/l$, solves the problem of selection rules and ω_L dependence, but not of the line shape, since $\mathrm{Im}F_j$ would be proportional to ω rather than ω^{-1}. Neither dependence agrees with experiment.

In view of the fact that the theory (Eq. 28) is inadequate in explaining the selection rules, line shape and exciting frequency dependence of the observed scattering, an attempt has not been made to account quantitatively for its behavior under uniaxial stress. Instead, the simple phenomenological model discussed above [removal of $Q_i Q_j$ in Eq. (28), leaving only the summation over the valleys for the difference in the inverse effective mass tensor] is used. Scattering is then allowed under valley-orbit selection rules, and a nonzero scattering cross section exists only if different components of the inverse effective mass tensor are picked up for the different valleys.

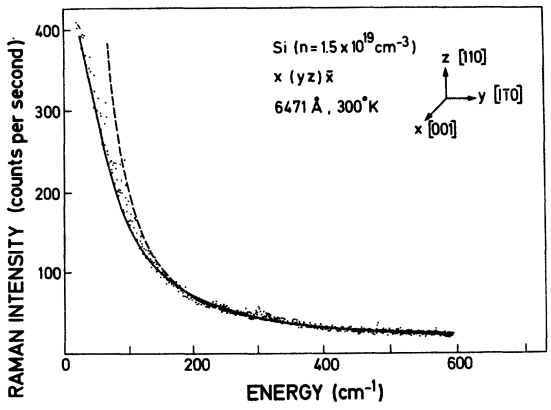

FIG. 2. Theoretical fits to the tail for Si, $n = 1.5\times10^{19}$ cm^{-3}, in the [110] [1$\bar{1}$0] polarization configuration, (001) face. The solid line is a fit to the *ad hoc* assumption of Eqs. (28a) and (28b), using $E_a = 8$ meV; the dashed line to $(1/\omega)(1+n_\omega)$. The dots are experimental Raman data at room temperature. The baseline and amplitude were adjusted for the best fit.

C. Effects of uniaxial stress

Large static uniaxial stresses (up to 20 kbars) were applied along three axes of high symmetry, the [001], [110], and [111] crystallographic directions. The resultant experimental data are shown in Figs. 3 to 8. The scattering configurations are indicated in the figures, in all cases $\hat{x}$ being the face used for scattering and $\hat{z}$ the direction of the uniaxial stress. All measurements were performed at 300 K, using 6471 Å exciting radiation. Measurements were performed on phosphorus-doped Si of concentrations $n = 1.5\times10^{19}$ cm^{-3} and $n = 1.5\times10^{20}$ cm^{-3}.

1. [001] stress

The application of a [001] uniaxial stress splits the three equivalent conduction band valleys into a singlet [001] along the stress and a doublet [100] and [010] perpendicular to the stress, the singlet being lower in energy. Consequently, the carriers are dumped into the singlet valley. In Table II, we list the various polarization configurations used (Column 2), the component μ_j of the reciprocal mass tensor $\vec{\mu}$ (for the particular polarization) for each of the valleys, labeled $j = 1, 2, 3$ ([100], [010], [001], respectively) (Column 3). Contribut-

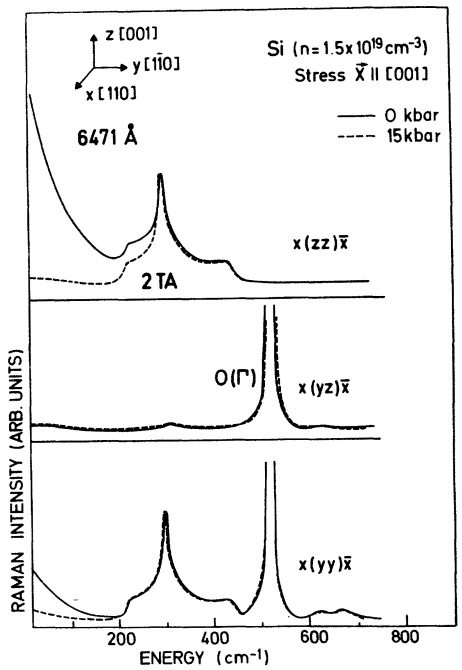

FIG. 3. Raman spectra of Si, $n = 1.5\times10^{19}$ cm^{-3}, under uniaxial stress along the [001] direction. Solid lines are zero-stress data, dashed lines at 15 kbar. The polarizations are indicated in the figure. Note the disappearance of the tail under stress.

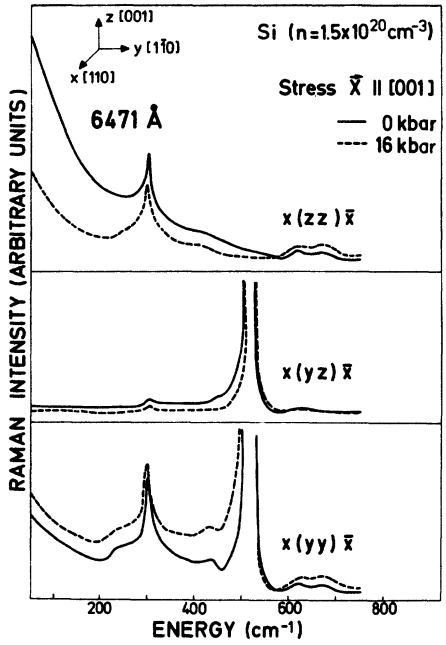

FIG. 4. Raman spectra of Si, $n = 1.5\times10^{20}$ cm^{-3}, under uniaxial stress along the [001] direction. Solid lines are at zero stress, dashed lines at 16 kbar. The polarizations are indicated in the figure.

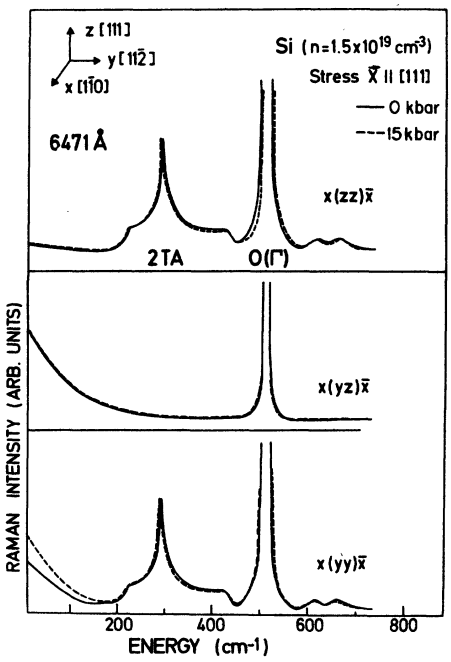

FIG. 5. Raman spectra of Si, $n = 1.5\times10^{19}$ cm^{-3}, under uniaxial stress along the [111] direction. Solid lines are at zero stress, dashed lines at 15 kbar. The polarizations are indicated in the figure.

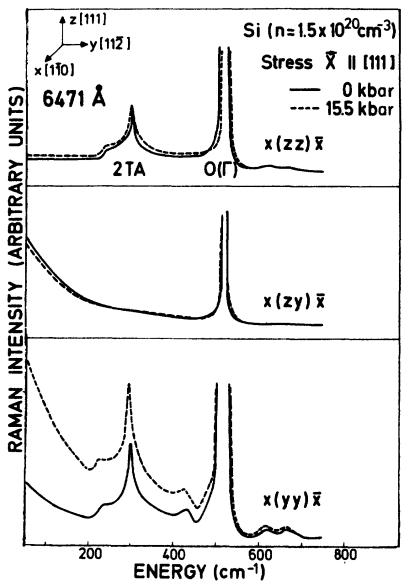

FIG. 6. Raman spectra of Si, $n = 1.5\times10^{20}$ cm^{-3}, under uniaxial stress along the [111] direction. Solid lines are at zero stress, dashed lines at 15.5 kbar. The polarizations are indicated in the figure.

ing pairs of valleys [those for which $(\mu_i - \mu_j) \neq 0$] are listed in Column 4, and the total contribution to the scattering, according to Eq. (29), is listed in Column 5. In this notation, valleys 1 and 2 are

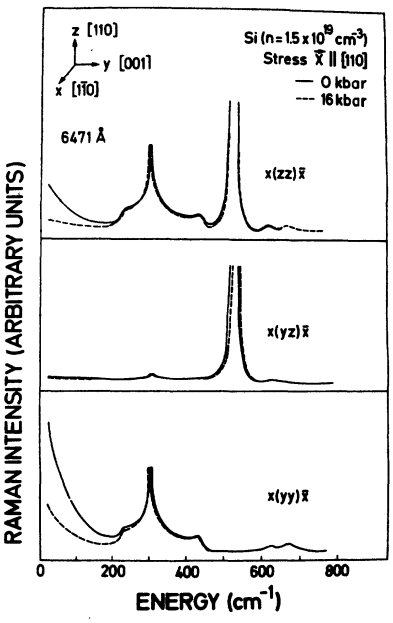

FIG. 7. Raman spectra of Si, $n = 1.5\times10^{19}$ cm^{-3}, under uniaxial stress along the [110] direction for the (1$\bar{1}$0) face. Solid lines are at zero stress, dashed lines at 16 kbar. The polarizations are indicated in the figure. The horizontal axis is linear in wavelength rather than wavenumber.

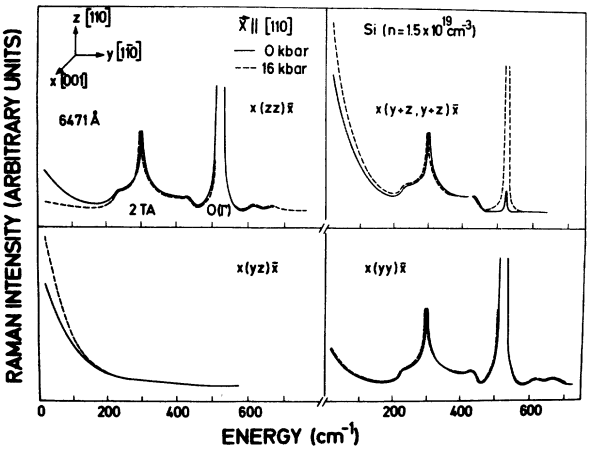

FIG. 8. Raman spectra of Si, $n = 1.5\times10^{19}$ cm^{-3}, under uniaxial stress along the [110] direction for the (001) face. Solid lines are at zero stress, dashed lines at 16 kbar. The high stress data do not change appreciably at 20 kbar. The polarizations are indicated in the figure. The horizontal axis is linear in wavelength rather than wave number.

the doublets that are depleted of carriers, and 3 is the enhanced singlet. A total dumping into the singlet valley would cause a disappearance of the tail for all polarizations, due to the requirement of having carriers in at least two valleys with different components of the inverse mass contributing to the scattering, while an incomplete transfer would decrease the strength of the tail. Column 6 indicates the direction the strength of the tail would be expected to take under stress, using only the simple model obtained from neglecting Q_iQ_j, Eq. (29).

The shear-induced shifts in energy for the singlet and doublet δE_s and δE_d, respectively, from the zero stress value, are given by

$$\delta E_s = -\tfrac{2}{3}\bar{X}\Xi_u(S_{11}-S_{12})$$
$$\delta E_d = \tfrac{1}{3}\bar{X}\Xi_u(S_{11}-S_{12}) \qquad (31)$$

where Ξ_u is the shear deformation potential, $\bar{X}$ is the magnitude of the applied stress, and S_{11}, S_{12} are elastic compliance constants. The splitting between the doublet and the singlet, $\delta E_d - \delta E_s$, calculated for values of $S_{11}-S_{12} = 1.01\times10^{-12}$ cm^2/dyn and $\Xi_u = 8.77\pm0.07$ eV is found to be 0.13 eV at 15 kbar.[12,13]

The fraction of the carriers dumped into the singlet valley depends on the concentration: at the lower doping $n = 1.5\times10^{19}$ cm^{-3}, the Fermi level at room temperature is at approximately

TABLE II. Effect of a [001] uniaxial stress on the intervalley fluctuations. The doublets depleted of carriers under stress are valleys 1 and 2 ([100] and [010] directions). The enhanced singlet valley 3 ([001] direction). The face used for scattering is [110]. Scattering intensity under stress is predicted by the model of Eq. (29).

$\vec{q}\,\|\,\hat{x}$ $\vec{X}\,\|\,\hat{z}$	Polarization configuration $\vec{q}(\vec{e}_1,\vec{e}_2)\vec{q}$	$\vec{e}_1\cdot\vec{\mu}_j\cdot\vec{e}_2=\mu_j$ $j=1,2,3$	Contributing pairs of valleys	Scattering intensity $R\sim\sum_{i,j}(\mu_i-\mu_j)^2$	Scattering intensity under stress
$\hat{x}=\frac{1}{\sqrt{2}}(1,1,0)$	$x(zz)\bar{x}$	$\mu_1=\frac{1}{m_t}$	1,3;	$2\left(\frac{1}{m_l}-\frac{1}{m_t}\right)^2$	Tail decreases with stress
$\hat{y}=\frac{1}{\sqrt{2}}(1,\bar{1},0)$	$\mu_j=\frac{1}{m^*_{izz}}$	$\mu_2=\frac{1}{m_t}$	2,3		
$\hat{z}=(0,0,1)$		$\mu_3=\frac{1}{m_l}$			
	$x(yz)\bar{x}$				No tail
	$\mu_j=0$				
	$x(yy)\bar{x}$	$\mu_1=\frac{1}{2}\left(\frac{1}{m_l}+\frac{1}{m_t}\right)$	1,3;	$\frac{1}{2}\left(\frac{1}{m_l}-\frac{1}{m_t}\right)^2$	Tail decreases with stress
	$\mu_j=\frac{1}{2}\left(\frac{1}{m^*_{ixx}}+\frac{1}{m^*_{iyy}}\right)$	$\mu_2=\frac{1}{2}\left(\frac{1}{m_l}+\frac{1}{m_t}\right)$	2,3		
		$\mu_3=\frac{1}{m_t}$			

21 meV above the conduction band minimum at zero stress, and the singlet-doublet splitting of 0.13 eV at 15 kbar effects total dumping into the singlet valley. The tail, which is seen for the $x(zz)\bar{x}$ and $x(yy)\bar{x}$ configurations (Fig. 3) at zero stress (solid lines), totally disappears at high stress (dashed lines). For the higher doping, 1.5×10^{20} cm^{-3}, the zero-stress Fermi level is approximately 0.1 eV at room temperature, and the transfer of carriers is incomplete at 16 kbar. The intensity of the tail for the (zz) polarization is reduced (Fig. 4) but does not go to zero, while for the (yy) polarization it remains approximately the same as for zero stress. In Fig. 4, the line shape of the optical phonon is asymmetric on the low-frequency side due to Fano-type interference with the electronic interband scattering. The stress induced filling of the singlet valley increases this asymmetry for the (yy) polarization.[6] This probably accounts for the upward shift with stress of the low-frequency tail in the (yy) configuration in Fig. 4.

2. [111] stress

Under [111] uniaxial stress the three conduction-band valleys remain equivalent, and the tail is expected not to change with stress. At the lower doping (Fig. 5), the tail in the (yz) configuration does indeed remain the same with stress (solid and dashed lines at 0 and 16 kbar, respectively) but for the (yy) configuration a slight increase is seen. In Fig. 6, for the higher doping, the tail in the (yz) configuration is again unchanged while in the (yy) configuration it increases strongly with stress (dashed lines).

The increase in the tail for the (yy) polarizations suggests nonparabolicity (energy density fluctuation) effects due to the splitting of the bands at the X_1 point. Particularly for the higher doping, where the Fermi level is close to the X_1 point at zero stress, the effects of the nonparabolicity are expected to be large when the X_1 point splits under stress. Unscreened "intervalley" scattering can then take place within a single valley. In view of the strong nonparabolicity at X_1, this effect can be quite strong.

For the lower doping, the effects of nonparabolicity due to the splitting of the X_1 point are expected to be much smaller because of the lower Fermi energy. In this case, if the nonparabolicity is neglected in the absence of stress, the splitting of the X_1 point by the [111] stress breaks down, to the first order in stress, the symmetry of revolution of the constant energy surfaces: the mass ellipsoids develop anisotropic transverse masses.[11] Calculations (see Appendix B) indicate that the difference $(\mu_i-\mu_j)^2_{yy}$ increases with compressive [111] stress for the (yy) configuration, thus yielding according to Eq. (B8) a slight increase of scattering efficiency with stress, in agreement with experiment. By the same token, the scattering efficiency for the (yz) configuration is expected to decrease. The magnitude of the change in $(\mu_i-\mu_j)_{yz}$ is, however, half as much as that for $(\mu_i-\mu_j)_{yy}$. The decrease in the scattering efficiency for the (yz) polarization is therefore about four times smaller than the increase for the (yy) polarization. It probably lies within the limits of experimental error for the (yz) configuration for the lower doping in Fig. 5, but it predicts in the case of $n=1.5\times10^{20}$ cm^{-3} a larger decrease than observed for the (yz) configuration in Fig. 6 (see Appendix B). For the case of the higher doping, however, nonparabolic effects are expected to dominate over effects due to the transverse mass anisotropy.

3. [110] stress

A [110] uniaxial stress splits the equivalent valleys into a doublet [100] and [010], and a singlet [001], the doublet being lower in energy. The shear-induced energy shifts of the doublet and singlet, $\delta E_d'$ and $\delta E_s'$, respectively, are

$$\delta E_d' = -\tfrac{1}{6}\Xi_u \bar{X}(S_{11}-S_{12}),$$
$$\delta E_s' = \tfrac{1}{3}\Xi_u \bar{X}(S_{11}-S_{12}). \tag{32}$$

The doublet-singlet splitting $(\delta E_s' - \delta E_d')$ is consequently half of the splitting for an equivalent [001] stress, besides being inverted in energy ordering.

Figures 7 and 8 present the effects of [110] stress on scattering intensity, both at zero stress (solid lines) and high stress (dashed lines) for the two faces used, $(1\bar{1}0)$ and (001), for samples of lower doping (1.5×10^{19} cm^{-3}).

With the $(1\bar{1}0)$ face the tails for the (zz) and (yy) polarizations are expected to decrease with stress (Table III). The (yy) polarization is seen not to have totally disappeared with stress (Fig. 7) indicating an incomplete transfer of carriers into the doublet valleys. This is not surprising since the splitting between the doublet and singlet is half that for [001] stress (0.07 eV at 16 kbar), and thus insufficient to transfer all the carriers to the lower doublet. A simple calculation based on Maxwell Boltzmann statistics[14] indicates that about 10% of the original number of carriers are still left in the singlet valley at 16 kbar. According to Table III the (zz) polarization is expected to decrease under stress and is seen in fact to totally disappear (Fig. 7) in spite of the incomplete transfer of carriers, as suggested by the (yy) configuration.

TABLE III. Effect of a [110] uniaxial stress on the intervalley fluctuations. The singlet, depleted of carriers is 3, ([001] direction) and the enhanced doublets are 1 and 2, ([100] and [010] directions). The face used for scattering is $(1\bar{1}0)$. Scattering intensity under stress is predicted by the model of Eq. (29).

$\vec{q}\parallel\hat{x}$ $\vec{X}\parallel\hat{z}$	Polarization configuration $\vec{q}(\vec{e}_1\vec{e}_2)(-\vec{q})$	$\vec{e}_1\cdot\vec{\mu}_j\cdot\vec{e}_2=\mu_j$ $j=1,2,3$	Contributing pairs of valleys	Scattering intensity $R\sim\sum_{i,j}(\mu_i-\mu_j)^2$	Scattering intensity under stress
$\hat{x}=\frac{1}{\sqrt{2}}(1,\bar{1},0)$	$x(zz)\bar{x}$	$\mu_1=\frac{1}{2}\left(\frac{1}{m_l}+\frac{1}{m_t}\right)$	1,3;	$\frac{1}{2}\left(\frac{1}{m_t}-\frac{1}{m_l}\right)^2$	Tail decreases with stress
$\hat{y}=(0,0,1)$	$\mu_j=\frac{1}{2}\left(\frac{1}{m^*_{lxx}}+\frac{1}{m^*_{lyy}}\right)$	$\mu_2=\frac{1}{2}\left(\frac{1}{m_l}+\frac{1}{m_t}\right)$	2,3		
$\hat{z}=\frac{1}{\sqrt{2}}(1,1,0)$		$\mu_3=\frac{1}{m_t}$			
	$x(zz)\bar{x}$				No tail
	$\mu_j=0$				
	$x(yy)\bar{x}$	$\mu_1=\frac{1}{m_t}$	1,3;	$2\left(\frac{1}{m_t}-\frac{1}{m_l}\right)^2$	Tail decreases with stress
	$\mu_j=\frac{1}{m^*_{lzz}}$	$\mu_2=\frac{1}{m_t}$	2,3		
		$\mu_3=\frac{1}{m_l}$			

The reason for this probably lies in the fact that the [001] X_1 point is split under [110] stress, and an anisotropy in the transverse mass is introduced. As will be discussed later on in this section in connection with the behavior of the tail as seen on the (001) face, the decrease of the tail is speeded up due to the transverse mass anisotropy.

For the (001) face (Fig. 8), in addition to the usual three polarizations, a fourth configuration $(y+z,y+z)$ at 45° to the stress, along the [100] direction, was measured. It should be noted that the four configurations are not independent. The extra $(y+z,y+z)$ configuration was measured in order to observe the doublet-doublet interaction more closely.

The expected behavior of the free-electron tail for various polarizations under stress, using the simple model [Eq. (29), less Q_iQ_j terms], not including effects of transverse mass anisotropy, is given in Table IV. As indicated in the table, the (yz) and the $(y+z,y+z)$ polarizations have two competitive mechanisms, one component between the doublet and singlet that decreases with stress, and one between the doublets that increases with stress, due to the increased number of carriers in the doublet valleys. At a stress of 16 kbar, the increase is seen to be the dominant feature (Fig. 8). If complete transfer had taken place, the doublet-doublet component alone would remain, which is equal for both (yz) and $(y+z,y+z)$ configurations. Experimentally, however, it is observed that the scattering for the two configurations are not equal at high stress (Fig. 8), providing additional evidence for the incomplete transfer of carriers. The data as shown at 16 kbar in Fig. 8 do not change appreciably at 20 kbar. For the (yy) polarization, in principle equivalent to the (zz) (Table IV), the tail is expected to decrease with stress. However, contributions from the anisotropy of the transverse mass due to stress[11] come in (see Appendix B). A pictorial representation of the behavior of the mass ellipsoids due to splitting of the [001] X_1 point under [110] stress is provided in Fig. 9(b). The doublets, the [100] and [010] valleys, labeled 1 and 2, gain carriers with stress, while valley 3 is depleted. The split X_1 point at valley 3 destroys the equivalence of the two transverse masses so that the larger transverse mass is pointed along the stress direction, and the smaller one perpendicular to it [dashed ellipsoid in valley 3, Fig. 9(b)]. This causes the scattering intensity of the tail to decrease slower with stress for the (yy) than the (zz) polarization (Appendix B), thus preserving the tail for the (yy) configuration

TABLE IV. Effect of a [110] uniaxial stress on the intervalley fluctuations. The singlet, depleted of carriers is 3, ([001] direction) and the enhanced doublets are 1 and 2, ([100] and [010] directions). The face used is (001). Scattering intensity under stress is predicted by the model of Eq. (29).

$\vec{q}\parallel\hat{x}$ $\vec{X}\parallel\hat{z}$	Polarization configuration $\vec{q}(\vec{e}_1\vec{e}_2)(-\vec{q})$	$\vec{e}_1\cdot\vec{\mu}_j\cdot\vec{e}_2=\mu_j$ $j=1,2,3$	Contributing pairs of valleys	Scattering intensity $R\sim\sum_{i,j}(\mu_i-\mu_j)^2$	Scattering intensity under stress
$\hat{x}=(0,0,1)$	$x(zz)\bar{x}$	$\mu_1=\frac{1}{2}\left(\frac{1}{m_l}+\frac{1}{m_t}\right)$	1,3;	$\frac{1}{2}\left(\frac{1}{m_t}-\frac{1}{m_l}\right)^2$	Tail decreases with stress
$\hat{y}=\frac{1}{\sqrt{2}}(1,\bar{1},0)$	$\mu_j=\frac{1}{2}\left(\frac{1}{m^*_{ixx}}+\frac{1}{m^*_{iyy}}\right)$	$\mu_2=\frac{1}{2}\left(\frac{1}{m_l}+\frac{1}{m_t}\right)$	2,3		
$\hat{z}=\frac{1}{\sqrt{2}}(1,1,0)$		$\mu_3=\frac{1}{m_t}$			
	$x(yz)\bar{x}$	$\mu_1=\frac{1}{2}\left(\frac{1}{m_l}-\frac{1}{m_t}\right)$	1,2;		Contribution from 1,2 increases and from 1,3 and 2,3 decreases
	$\mu_j=\frac{1}{2}\left(\frac{1}{m^*_{ixx}}-\frac{1}{m^*_{iyy}}\right)$	$\mu_2=\frac{1}{2}\left(\frac{1}{m_t}-\frac{1}{m_l}\right)$	2,3;	$\frac{3}{2}\left(\frac{1}{m_t}-\frac{1}{m_l}\right)^2$	
		$\mu_3=0$	1,3		
	$x(y+z,y+z)\bar{x}$	$\mu_1=\frac{1}{m_l}$	1,2;	$2\left(\frac{1}{m_t}-\frac{1}{m_l}\right)^2$	Contribution from 1,2 increases, and 1,3 decreases with stress
	$\mu_j=\frac{1}{m^*_{ixx}}$	$\mu_2=\frac{1}{m_t}$	1,3		
		$\mu_3=\frac{1}{m_t}$			
	$x(yy)\bar{x}$	$\mu_1=\frac{1}{2}\left(\frac{1}{m_l}+\frac{1}{m_t}\right)$	1,3;	$\frac{1}{2}\left(\frac{1}{m_t}-\frac{1}{m_l}\right)^2$	Tail decreases with stress
		$\mu_2=\frac{1}{2}\left(\frac{1}{m_l}+\frac{1}{m_t}\right)$			
	$\mu_j=\frac{1}{2}\left(\frac{1}{m^*_{ixx}}+\frac{1}{m^*_{iyy}}\right)$	$\mu_3=\frac{1}{m_t}$	2,3		

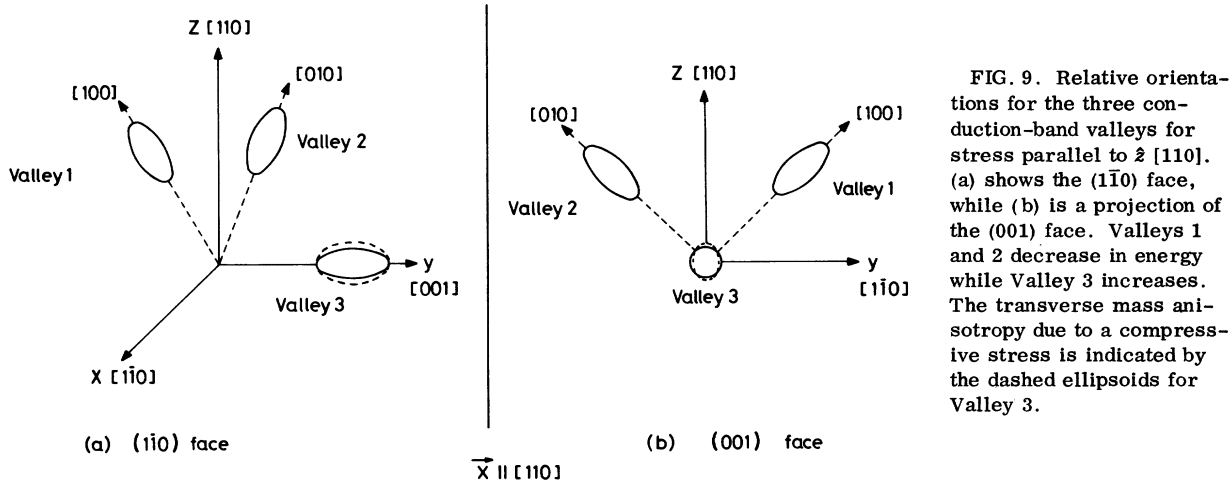

FIG. 9. Relative orientations for the three conduction-band valleys for stress parallel to $\hat{z}$ [110]. (a) shows the (1$\bar{1}$0) face, while (b) is a projection of the (001) face. Valleys 1 and 2 decrease in energy while Valley 3 increases. The transverse mass anisotropy due to a compressive stress is indicated by the dashed ellipsoids for Valley 3.

(Fig. 8), while the tail has diminished considerably for the (zz) configuration, in spite of the incomplete transfer of carriers to the doublets as indicated by the other two polarizations, (yz) and $(y+z, y+z)$. It should be noted that contributions due to the anisotropy of the transverse masses do not enter into the (yz) and $(y+z, y+z)$ configurations, due to an exact cancellation of the terms involved. These two polarizations are accounted for using the model of Eq. (29).

The case of the (zz) configuration for the $(1\bar{1}0)$ face is the same as for the (001) face. The increased transverse mass along the stress direction decreases the differences $(\mu_1 - \mu_3)_{zz}$ or $(\mu_2 - \mu_3)_{zz}$ and speeds up the decrease in the strength of the tail in spite of the incomplete carrier transfer. The (yy) configuration is unaffected since it picks up the longitudinal component of the mass in valley 3 [see Fig. 9(a)].

It is also noticed, for the $(y+z, y+z)$ configuration (Fig. 8) that the zone center phonon at 520 cm^{-1}, which is disallowed for zero stress, gains intensity and becomes weakly allowed at high stresses, presumably due to stress induced birefringence. We believe this effect can be used to study the shear piezoelastic constants in the region where the material is opaque.[15]

D. Dependence on exciting frequency

We have also investigated the dependence of the free-carrier scattering tail on exciting frequency. A polarization was chosen so that only the tail and the zone center optical phonon appear. Frequencies smaller than 2.5 eV, away from the E_0 resonance at 3.4 eV were used.[16] For these frequencies the scattering by optical phonons is known to have an ω_L^4 dependence, where ω_L is the frequency of the exciting laser. The relative intensity of the free electron tail to that of the phonon divided by ω_L^4, is plotted in Fig. 10 for the highly doped sample (1.5×10^{20} cm^{-3}). The intensity of the tail was measured at two points, 50 and 120 cm^{-1} from the laser frequency. Figure 10 shows that the ratio has no frequency dependence, and therefore, in view of the constancy of $I(\text{phonon})/\omega_L^4$, the electronic scattering intensity has no frequency dependence.

A comparison was also made between the tail and the intensity of the interband excitations that produce the Fano interference with the Raman active phonon. The representative strength of these transitions was taken to be proportional to the difference between the background levels on the low- and high-frequency sides of the optical phonon. A plot of the relative intensities of the tail and the interband excitations is seen to give, again, no

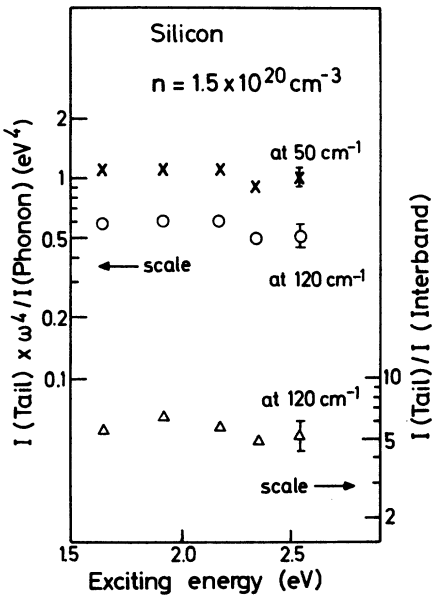

FIG. 10. Intensity of the tail relative to the zone-center optical phonon as a function of exciting energy for Si, $n = 1.5\times10^{20}$ cm^{-3}. The intensity of the phonon is compensated for its ω_L^4 dependence. The tail is measured at 50 cm^{-1} (×) and 120 cm^{-1} (○). The intensity of the tail relative to the intensity of interband excitations is also plotted (△) as a function of exciting energy. Measurements were made at room temperature.

frequency dependence; the scattering by interband excitations also seems to be frequency independent.

It has been shown by Zeyher *et al.*[17] that the ω_L^4 dependence of the scattering efficiency only appears at frequencies ω_L small compared with those of *possible electronic excitations*. Such a factor is not expected for free-carrier scattering in a solid since there are electronic excitations of *zero frequency*. For both inter- and intraband scattering by free electrons in Si, the electronic virtual transitions involved are dominated by a term involving the X_4 valence band (or actually the Δ_5 valence state which corresponds to the Δ_1 minimum; this state is very close to X_4) as an intermediate state. In this case the scattering intensity has the following resonant behavior[5]

$$I \sim \left| \frac{\omega_2}{\omega_2 - \omega_L} \right|^2 \quad \text{for} \quad \omega_L < \omega_2 , \tag{33}$$

where ω_2 is the energy of the $\Delta_5 - \Delta_1$ gap (close to 4 eV in Si). According to Eq. (33) the scattering intensity for the electronic processes under consideration becomes constant for $\omega_L \ll \omega_2$ in agreement with our observations.

Contrary to the experimental observations Eq. (28) predicts a scattering efficiency proportional to ω_L^2. Both *ad hoc* expressions, that of Eq. (28a),

and that obtained by replacing q by $2\pi/l$ into the Q_j's [Eq. (22)] required to evaluate Eq. (28), yield a scattering efficiency independent of ω_L and in agreement with observations.

E. Scattering efficiency

The absolute scattering efficiency for the intervalley fluctuation mechanism can be calculated using Eq. (28). A similar calculation can be made for the optical phonon. In this section, we calculate the theoretical relative scattering efficiencies for the phonon with respect to the intervalley fluctuations, and compare it to experiment for a chosen configuration.

The efficiency for first-order scattering by optical phonons of frequency $\omega_0 = 520$ cm^{-1} can be obtained from the equation[18]

$$\left(\frac{d^2R}{d\omega\, d\Omega}\right)_{\rm ph} = \left(\frac{\omega_L}{c}\right)^4 (1+n_{\omega_0}) \frac{\hbar}{2\rho\omega_0} \left(\frac{8}{a_0 3}\right)^2 P^2 \times \left| \sum_{i=1}^{3} \hat{e}_1 \cdot \vec{T}_i \cdot \hat{e}_2 \right|^2 \delta(\omega - \omega_0), \quad (34)$$

where ρ is the density of the crystal, a_0 the lattice parameter, and P the polarizability derivative as defined by Swanson and Maradudin.[19] The value calculated by them[19] is $P = 22$ Å^2 at $\omega_L = 1.92$ eV, a value believed to be reliable in view of the results in Ref. 16. The three matrices T_i are

$$T_1 = \begin{pmatrix} 0 & 0 & 1 \\ 0 & 0 & 0 \\ 1 & 0 & 0 \end{pmatrix}, \quad T_2 = \begin{pmatrix} 0 & 0 & 0 \\ 0 & 0 & 1 \\ 0 & 1 & 0 \end{pmatrix},$$

$$T_3 = \begin{pmatrix} 0 & 1 & 0 \\ 1 & 0 & 0 \\ 0 & 0 & 0 \end{pmatrix}. \quad (35)$$

For the configuration

$$\hat{e}_1 = \frac{1}{\sqrt{3}}(1,1,1),$$

$$\hat{e}_2 = \frac{1}{\sqrt{6}}(1,1,\bar{2}), \quad (36)$$

$$\hat{q} = \frac{q}{\sqrt{2}}(1,\bar{1},0),$$

we obtain from Eq. (34) for the efficiency of scattering by optical phonons

$$\left(\frac{d^2R}{d\omega\, d\Omega}\right)_{\rm ph} = 8.85\times10^{-7}\,\delta(\omega-\omega_0)\ \text{rad}^{-1} \quad (37)$$

per unit scattering length, with all frequencies in cm^{-1}.

The scattering efficiency as defined by Eq. (28) for the sample with $n_0 = 1.5\times10^{19}$ cm^{-3} at a frequency $\omega = 50$ cm^{-1} yields for the electronic scattering efficiency per unit length

$$\left(\frac{d^2R}{d\omega\, d\Omega}\right)_e = 4.37\times10^{-10}\,\text{rad}^{-1} \quad (38)$$

for the configuration defined by Eq. (36).

The ratio of the *integrated intensity* of the phonon to the *height* of the electronic continuum thus becomes

$$r_{\text{ph},e} = \int_0^\infty \left(\frac{d^2R}{d\omega\, d\Omega}\right)_{\rm ph} \left(\frac{d^2R}{d\omega\, d\Omega}\right)_e^{-1} d\omega = 2.0\times10^3\ \text{cm}^{-1}. \quad (39)$$

The experimental value for $r_{\text{ph},e}$ obtained by analyzing the configuration of Eq. (36), $x(yz)\bar{x}$ in Fig. 5, is 140 cm^{-1}, an order of magnitude smaller than that of Eq. (39). We therefore conclude that Eq. (28) underestimates the efficiency of scattering by intervalley fluctuations. As already hinted in Sec. IV B, we can remedy some of the shortcomings of Eq. (28), especially those connected with the selection rules and ω_L, by replacing q by $2\pi/l$, with l equal to the mean-free path, removing all the angular dependence of Q_i. With the parameters given in Sec. III, $l = V_F\tau_{EF}$ where V_F is the Fermi velocity, yields $l = 25$ Å, and $2\pi/l = 2.5\times10^7$ cm^{-1}, which is much larger than $q = 7.5\times10^5$ cm^{-1}, at the exciting energy of 1.92 eV. Equation (28) thus predicts, upon substituting q by $2\pi/l$,

$$\left(\frac{d^2R}{d\omega\, d\Omega}\right)_e = 1.1\times10^{-7}\,\text{rad}^{-1}. \quad (40)$$

Equations (37), (39), and (40) yield $r_{\text{ph},e} = 8.0$ cm^{-1}, a value which is now smaller than the experimental one. We thus realize that the experimental $r_{\text{ph},e}$ lies half way between the theoretical predictions for $q = 4\pi n/\lambda_L$ and those for the symmetrized $q = 2\pi/l$. We believe this result lends further plausibility to our explanation of the shortcomings of Eq. (28).

We should also point out that the use of Eq. (28a) with $a_0 = 1$ and $E = 8$ meV gives a value of $r_{\text{ph},e} = 4\times10^3$ cm^{-1} at $\omega = 50$ cm^{-1}, a disagreement worse than the one obtained if one retained the angular factors of Eq. (28). An *ad hoc* value of $a_0 \simeq 0.05$ would yield the experimentally observed $r_{\text{ph},e}$.

V. CONCLUSIONS

In this study we have investigated intraband free-electron Raman scattering in silicon, at concentrations of 1.5×10^{19} cm^{-3} and 1.5×10^{20} cm^{-3}. The strong low-frequency tails observed are seen to behave in terms of selection rules, line shapes, and exciting frequency dependences in a manner not justifiable by the free-electron theoretical approach usually used in describing heavily doped semiconductors. This intervalley electron density

fluctuation theory, used in *ad hoc* modified forms that neglect the effects of $\vec{q}$, the momentum transfer, is able to account for the selection rules, the dependence on exciting frequency and the line shape. These modified forms, however, cannot be justified on theoretical grounds. The simplified models are also used quite effectively to explain most of the behavior of the tail under uniaxial stress, in conjunction with effects due to transverse effective mass anisotropy produced by the splitting of X_1 points under [110] and [111] stresses. In such cases, nonparabolic effects are also expected to be strong, and somewhat difficult to handle theoretically.

While it is clear that the free-electron approach cannot completely justify the experimental behavior, other possibilities, such as using a partly localized approach exist; it is hoped that this work will stimulate more theoretical interest in this area.

ACKNOWLEDGMENTS

The authors would like to thank Dr. J. B. Renucci for help in the measurements made during the early stages of this work, Dr. D. E. Aspnes for providing the 10^{20}-cm^{-3} crystal, and A. Kaiser and G. Fröhlich for orienting and polishing the samples.

APPENDIX A: DERIVATION OF THE TRANSPORT EQUATION

We wish to extend the derivation of the Liouville equation for transport in the presence of elastic impurity scattering which has been given by Kohn and Luttinger[9] for the case of a constant field.

We assume a time-varying potential

$$\phi(r,t)=\phi(q,\omega)e^{i\vec{q}\cdot\vec{r}-i\omega t} \tag{A1}$$

and calculate the Liouville equation for the system consisting of free electrons with dispersion $\mathcal{E}_{\vec{k}}$ together with an elastic impurity scattering potential $H_{\vec{k}\vec{k}'}$ whose diagonal elements are zero. We treat ϕ to first order.

We introduce a density matrix in momentum space $\rho(\vec{k}',\vec{k})e^{i\omega t}$, where ρ is the change in the equilibrium density matrix induced by $\phi(q,\omega)$. The standard form of the Liouville equations is

$$(\omega-\mathcal{E}_{\vec{k}+\vec{q}}+\mathcal{E}_{\vec{k}})\rho(\vec{k}+\vec{q},\vec{k})=[f_0(\mathcal{E}_{\vec{k}})-f_0(\mathcal{E}_{\vec{k}+\vec{q}})]\phi(q,\omega)+\sum_{\vec{k}'}H_{\vec{k}+\vec{q},\vec{k}'}\rho(\vec{k}',\vec{k})-\rho(\vec{k}+\vec{q},\vec{k}')H_{\vec{k}',\vec{k}}, \tag{A2}$$

where f_0 is the Fermi distribution function.

$$(\omega-\mathcal{E}_k+\mathcal{E}_{k'})\rho(k,k')=H_{k,k'+q}\rho(\vec{k}'+\vec{q},\vec{k}')-\rho(\vec{k},\vec{k}-\vec{q})H_{\vec{k}-\vec{q},k};\quad \vec{k}-\vec{k}'\neq\vec{q}\,. \tag{A3}$$

In Eq. (A3) we have made the approximation of keeping only the dominant terms $\rho(\vec{k},\vec{k}')$, $\vec{k}-\vec{k}'=\vec{q}$ on the right-hand side. This means that the scattering potential is assumed to be weak, a fact of dubious applicability in our case. We believe the problem in our treatment may be here. We then solve for $\rho(\vec{k},\vec{k}')$ from (A3) and substitute it in (A2). We also assume H is a sum of local potentials so that $H_{\vec{k},\vec{k}'}=H_{\vec{k}-\vec{k}'}$. Equation (A2) then becomes

$$(\omega-\mathcal{E}_{\vec{k}+\vec{q}}+\mathcal{E}_{\vec{k}})\rho(\vec{k}+\vec{q},\vec{k})=[f_0(\mathcal{E}_{\vec{k}})-f_0(\mathcal{E}_{\vec{k}+\vec{q}})]\phi(q,\omega)+\rho(\vec{k}+\vec{q},\vec{k})\sum_{\vec{k}'}w_{\vec{k},\vec{k}'}-\sum_{\vec{k}'}\rho(\vec{k}'+\vec{q},\vec{k}')w_{\vec{k},\vec{k}'}, \tag{A4}$$

where

$$w_{\vec{k},\vec{k}'}=|H_{\vec{k}-\vec{k}'}|^2\left(\frac{1}{\omega-\mathcal{E}_{\vec{k}'+\vec{q}}+\mathcal{E}_{\vec{k}}}+\frac{1}{\omega-\mathcal{E}_{\vec{k}+\vec{q}}+\mathcal{E}_{\vec{k}'}}\right). \tag{A5}$$

We then assume that the dominant part of w is the imaginary part coming from the poles and that ω and q are small so that w may be written

$$w_{\vec{k},\vec{k}'}=i2\pi|H_{\vec{k}-\vec{k}'}|^2\delta(\mathcal{E}_{\vec{k}}-\mathcal{E}_{\vec{k}'})\,. \tag{A6}$$

APPENDIX B: EFFECT OF THE STRESS INDUCED SPLITTING OF THE X_1 POINTS UNDER [110] AND [111] STRESS ON THE INTRABAND SCATTERING

The strain induced splitting of the X_1 point under a compressive uniaxial stress along [110] may be described by the $\vec{k}\cdot\vec{p}$ matrix[11]

$$\begin{bmatrix}\frac{k_x^2+k_y^2}{2m_t}-Ak_z & \frac{k_xk_y}{m_t}+\Delta\\ \frac{k_xk_y}{m_t}+\Delta & \frac{k_x^2+k_y^2}{2m_t}+Ak_z\end{bmatrix}, \tag{B1}$$

where 2Δ is the stress induced splitting of the X_1 point along the [001] direction,

$$A=\frac{1}{m}\langle X_1|p_z|X_1\rangle \tag{B2}$$

where p_z describes the electron momentum along the (001) direction and X_1 is the wave function describing the conduction bands. m_t is the transverse mass.

To first order in the stress, the eigenvalues of Eq. (B1) are

$$E=\frac{k_x^2+k_y^2}{2m_t}\pm\frac{\Delta k_xk_y}{Ak_zm_t}\pm Ak_z\,. \tag{B3}$$

The energy ellipsoid corresponding to the lower Δ_1 conduction band has the form

$$\frac{k_x^2+k_y^2}{2m_t}-\frac{\Delta k_x k_y}{Ak_z m_t}=E' \tag{B4}$$

which can be diagonalized to the new principal axes with different effective masses

$$\text{axis } \frac{1}{\sqrt{2}}(1,\bar{1},0) \text{ with } \frac{1}{m_t'}=\frac{1}{m_t}\left(1+\frac{\Delta}{Ak_z}\right)$$
$$\text{axis } \frac{1}{\sqrt{2}}(1,1,0) \text{ with } \frac{1}{m_t''}=\frac{1}{m_t}\left(1-\frac{\Delta}{Ak_z}\right) \tag{B5}$$

The sign of Δ is known to be positive,[11] while A and k_z are also positive. In this treatment, the stress dependence of m_t has been neglected, but can in fact be included using the known variation with stress.[11]

At high stress, the transverse elliptic cross section of the effective mass ellipsoid with its larger mass oriented along [110] is seen to have the following effect on intervalley fluctuations (Fig. 9). For a [110] stress, (001) face, the stress depletes the singlet valley of carriers. Let us consider the polarizations (zz) and (yy) which at zero stress are equivalent, and should show a decrease in the tail at an equal rate according to Table IV. Due to the increase of the transverse mass along [110], the (zz) polarization has a scattering intensity

$$R(zz)\sim\frac{1}{2}\left[\frac{1}{m_t}\left(1-\frac{\Delta}{Ak_z}\right)-\frac{1}{m_l}\right]^2, \tag{B6}$$

the decrease in the tail due to carrier transfer being helped by the decreasing difference in the inverse effective masses.

For the (yy) polarization, however,

$$R(yy)\sim\frac{1}{2}\left[\frac{1}{m_t}\left(1+\frac{\Delta}{Ak_z}\right)-\frac{1}{m_l}\right]^2 \tag{B7}$$

the decrease in the tail is hindered by the increasing difference in the effective masses.

The other polarizations for this face, $(y+z, y+z)$ and (yz) are not affected by the mass anisotropy. For the case of $\vec{X}\|[110]$, $(1\bar{1}0)$ face, the (zz) polarization is affected in a similar way as for the (zz) in the (001) face. The (yy) is unaffected since it picks up the longitudinal mass of the [001] ellipsoid.

The case of the [111] stress is complicated by the splitting of all three X_1 points under stress. The relevant terms can be calculated in a manner similar to the [110] stress, and the scattered intensities for the (yz) and (yy) polarizations are

$$R(yz)\sim\left[\frac{1}{m_t}\left(1-\frac{\Delta}{Ak_z}\right)-\frac{1}{m_l}\right]^2$$
$$R(yy)\sim\frac{1}{2}\left[\frac{1}{m_t}\left(1+\frac{2\Delta}{Ak_z}\right)-\frac{1}{m_l}\right]^2. \tag{B8}$$

The transverse mass anisotropy experimentally determined by Hensel *et al.*[11] gives a value of 1.01×10^{-2} kbar for Δ/Ak_z, from which it can be calculated that $R(yz)$ should decrease by about 35% at 16 kbar, while $R(yy)$ should increase by a factor of two. While the directions of the changes of the scattering intensity is correct for the (yy) configuration, the magnitudes are more than what is experimentally observed: in Fig. 5, the (yy) configuration increases by about 60%, while the (yz) configuration has no detectable decrease within experimental error.

The calculations just given are expected to be correct only in a region where nonparabolic effects can be neglected. It is expected, that for the higher doping of 1.5×10^{20} cm^{-3}, nonparabolic effects within a single valley should be much stronger, and will dominate, especially when the X_1 point is split by stress. However, it is also possible that for the lower doping contributions due to nonparabolicities exist.

---

†Formerly Meera Chandrapal.
*On leave from Bell Laboratories, Murray Hill, N.J.
Supported by the Alexander von Humboldt Foundation.

[1]M. Jouanne, R. Beserman, I. Ipatova, and A. Subashiev, Solid State Commun. 16, 1047 (1975).
[2]K. Jain, S. Lai, and M. V. Klein, Phys. Rev. B 13, 5448 (1976).
[3]J. Doehler, Phys. Rev. B 12, 2917 (1975).
[4]P. M. Platzman, Phys. Rev. 139, A379 (1965).
[5]M. V. Klein, *Light Scattering in Solids*, edited by M. Cardona (Springer-Verlag, New York, 1975).
[6]M. Chandrasekhar, J. B. Renucci, M. Cardona, and E. O. Kane, *Proceedings of the Thirteenth International Conference on the Physics of Semiconductors, Rome*, 1976, edited by F. G. Fumi, p. 255 (Tipografia Marves, Rome, 1977).
[7]H. Vogelmann and T. A. Fjeldly, Rev. Sci. Instr. 45, 309 (1974).
[8]S. M. Sze, *Physics of Semiconductor Devices* (Wiley-Interscience, New York, 1969).
[9]W. Kohn and J. M. Luttinger, Phys. Rev. 108, 590 (1957).
[10]N. D. Mermin, Phys. Rev. B 1, 2362 (1970).
[11]J. C. Hensel, H. Hasegawa, and M. Nakayama, Phys. Rev. 138, A225 (1965).
[12]J. J. Hall, Phys. Rev. 161, 756 (1967).
[13]V. J. Tekippe, H. R. Chandrasekhar, P. Fisher, and A. K. Ramdas, Phys. Rev. B 6, 2348 (1972); and references therein.
[14]See, for example, H. Fritzsche, Phys. Rev. 115, 336 (1959).
[15]M. Chandrasekhar and M. Cardona, unpublished.

[16]J. B. Renucci, R. N. Tyte, and M. Cardona, Phys. Rev. B 11, 3885 (1975).
[17]R. Zeyher, H. Bilz, and M. Cardona, Solid State Commun. 19, 57 (1976).
[18]A. Pinczuk and E. Burstein, *Light Scattering in Solids*, edited by M. Cardona (Springer-Verlag, New York, 1975).
[19]L. R. Swanson and A. A. Maradudin, Solid State Commun. 8, 859 (1970).